Water Recovery X-Ray Rocket grating spectrometer

Drew M. Miles
Samuel V. Hull
Ted B. Schultz
James H. Tutt
Mitchell Wages
Benjamin D. Donovan
Randall L. McEntaffer
Abraham D. Falcone
Tyler Anderson
Evan Bray
David N. Burrows
Tanmoy Chattopadhyay
Chad M. Eichfeld
Nathan Empson
Fabien Grisé
Christopher R. Hillman
Jake A. McCoy
Maria McQuaide
Bailey J. Myers
Tyler Steiner
Marc A. Verschuuren
Daniel Yastishock
Ningxiao Zhang

SPIE.

Water Recovery X-Ray Rocket grating spectrometer

Drew M. Miles,[a,*] **Samuel V. Hull,**[a] **Ted B. Schultz,**[a] **James H. Tutt,**[a] **Mitchell Wages,**[a] **Benjamin D. Donovan,**[a]
Randall L. McEntaffer,[a] **Abraham D. Falcone,**[a] **Tyler Anderson,**[a] **Evan Bray,**[a] **David N. Burrows,**[a]
Tanmoy Chattopadhyay,[a] **Chad M. Eichfeld,**[a,b] **Nathan Empson,**[c] **Fabien Grisé,**[a] **Christopher R. Hillman,**[a]
Jake A. McCoy,[a] **Maria McQuaide,**[a] **Bailey J. Myers,**[a] **Tyler Steiner,**[a] **Marc A. Verschuuren,**[d]
Daniel Yastishock,[a] **and Ningxiao Zhang**[a]
[a]Pennsylvania State University, University Park, Department of Astronomy and Astrophysics, Pennsylvania, United States
[b]Pennsylvania State University, Materials Research Institute, Pennsylvania, United States
[c]NASA Sounding Rockets Program Office, Wallops Flight Facility, Wallops Island, Virginia, United States
[d]Philips SCIL Nanoimprint Solutions, Eindhoven, The Netherlands

Abstract. The Water Recovery X-Ray Rocket (WRXR) was a suborbital rocket payload that was launched and recovered in April 2018. The WRXR flew two technologies being developed for future large x-ray missions: x-ray reflection gratings and a hybrid CMOS detector (HCD). The large-format replicated gratings on the WRXR were measured in ground calibrations to have absolute single-order diffraction efficiency of ~60%, ~50%, and ~35% at CVI, OVII, and OVIII emission energies, respectively. The HCD was operated with ~6 e⁻ read noise and ~88 eV energy resolution at 0.5 keV. The WRXR was also part of a two-payload campaign that successfully demonstrated NASA sounding rocket water recovery technology for science payloads. The primary instrument, a soft x-ray grating spectrometer, targeted diffuse emission from the Vela supernova remnant over a field-of-view >10 deg². The flight data show that the detector was operational during flight and detected x-ray events from an on-board calibration source, but there was no definitive detection of x-ray events from Vela. Flight results are presented along with a discussion of factors that could have contributed to the null detection. © 2019 Society of Photo-Optical Instrumentation Engineers (SPIE) [DOI: 10.1117/1.JATIS.5.4.044006]

1 Introduction

The Water Recovery X-Ray Rocket (WRXR) was a suborbital rocket payload that launched from the Kwajalein Atoll on April 4, 2018. The WRXR was a technology-driven astrophysics payload that sought to demonstrate the performance of two technologies assigned the highest priority to NASA Astrophysics technology development in the 2019 Astrophysics Biennial Technology Report:[1] x-ray reflection gratings and an x-ray hybrid CMOS detector (HCD). Both technologies were studied or are actively under development for the Lynx flagship mission concept,[2–4] explorer and probe mission concepts,[5–8] and smaller missions, such as suborbital rocket payloads[9,10] and cubesats.[11] The WRXR, along with the Colorado High-resolution Echelle Stellar Spectrograph,[12] also enabled the first successful demonstrations of NASA water recovery technology for astrophysics suborbital rocket payloads. Further, the WRXR served as a pathfinder for an upcoming rocket-borne diffuse soft x-ray spectrometer that will improve in both effective area and spectral resolving power.

The WRXR spectrometer was designed to fill the gap in soft x-ray studies between observatories with small fields-of-view (FoV), such as the Chandra X-Ray Observatory and XMM-Newton, and instruments with a large FoV but poor energy resolution, such as ROSAT, SAS-3, and previous sounding rockets. The WRXR's observation target was the Vela supernova remnant (SNR), from which the WRXR sought to obtain the most highly resolved spectrum of Vela's diffuse soft x-ray emission. The spectrometer had a FoV of >10 deg² and resolving power of $\lambda/\delta\lambda \sim 40$ in Vela's dominant emission lines: OVII, OVIII, and CVI.

1.1 Instrument Overview

The WRXR's large FoV was enabled by a passive focuser that consisted of a series of electroformed nickel plates, each with 185 slits.[13] The overall FoV allowed by the focuser geometry was 3.32 deg × 17.6 deg. However, the angular extent of the Vela SNR, grating diffraction effects, and detector extent at the focal plane limited the total instrument FoV to ~13 deg². The widths of the slits and of the supporting frame that separates the slits converged over the 0.9-m length of the focuser system to produce a single line spread function (LSF) at the focal plane. The focuser LSF, therefore, consisted of an overlapping LSF from each of the 185 slits with a ~2 mm full width at half maximum (FWHM).

Immediately following the focuser in the spectrometer was an array of x-ray reflection gratings. The grating array covered the full exit aperture of the focuser and thereby intercepted and redirected focused x-rays to a diffraction arc at the focal plane. An x-ray HCD, developed as part of a collaboration between Penn State University (PSU) and Teledyne Imaging Sensors,[14,15] was used to image the diffracted spectral lines. The WRXR HCD was 36.9 mm × 36.9 mm, which was sufficient to capture the four target emission lines (CVI, OVIII, and two orders of OVII) but covered only ~20% of the lines' extent in the cross-dispersion direction. To improve instrument FoV and the effective area, an array of Ni-coated mirrors was installed after the grating array to provide a secondary reflection for diffracted
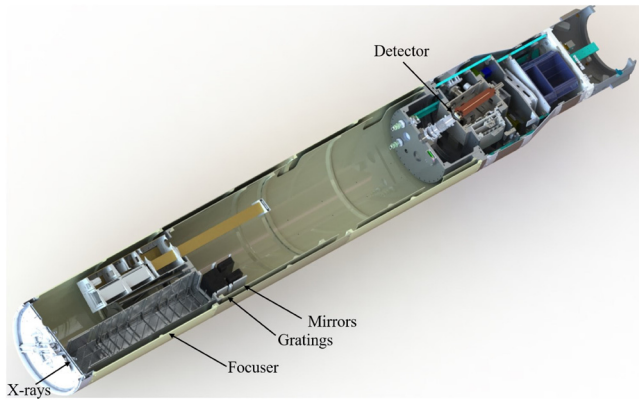
Fig. 1 A CAD model of the complete WRXR science payload. The components of the spectrometer are labeled.

photons. The mirror array was designed to reflect a portion of the photons that would fall outside the detector coverage onto the 36.9-mm active area, increasing instrument throughput by ~20%. A computer-aided design (CAD) model of the WRXR science payload is shown in Fig. 1 with the primary spectrometer components labeled.

1.2 Observation Target

The WRXR spectrometer's observation target was the diffuse soft x-ray emission from the northern part of the Vela SNR. The northern region was selected to observe a relatively unexplored area of Vela while simultaneously avoiding contamination from the Vela pulsar near the center of the remnant and the two other SNRs near Vela: Puppis A and Vela Jr.

The Vela SNR is a shell-type remnant at a distance of ~250 pc[16] and with an apparent diameter of ~8 deg. The morphology of Vela suggests that the local interstellar medium has been swept up by the precursor wind and supernova blast wave into a nearly spherical zone of interaction. Shock-heated plasmas in this zone reach collisional ionization equilibrium on a timescale that is inversely proportional to density; the denser regions, therefore, equilibrate more quickly and cool more efficiently than rarified regions, which remain hot and have emission at higher energies. This scenario is also seen in other type II shell remnants[17,18] and a spectrum of the broad emission in the northern part of the remnant will provide a basis for comparison among various shell-type remnants.

Vela's large apparent size, high surface brightness, and low intervening hydrogen column density have made the remnant a common target for both sounding rockets[19–21] and space telescopes.[22–26] However, previous studies have yielded some inconsistencies about the prevailing conditions across the remnant; most authors conclude that ionization equilibrium conditions exist (though with different proposed temperature models), but some observations suggest that a second temperature component or nonequilibrium conditions exist to an undetermined extent. Additionally, previous observations suffer from either prohibitively low spectral resolving power (sounding rockets and ROSAT) or a small FoV. The WRXR sought to combine a large FoV and moderate resolving power to perform an observation on the northern part of the remnant.

2 Optical Components

The light-collecting component of the WRXR spectrometer, a mechanical focuser that passively focused incident x-rays, was
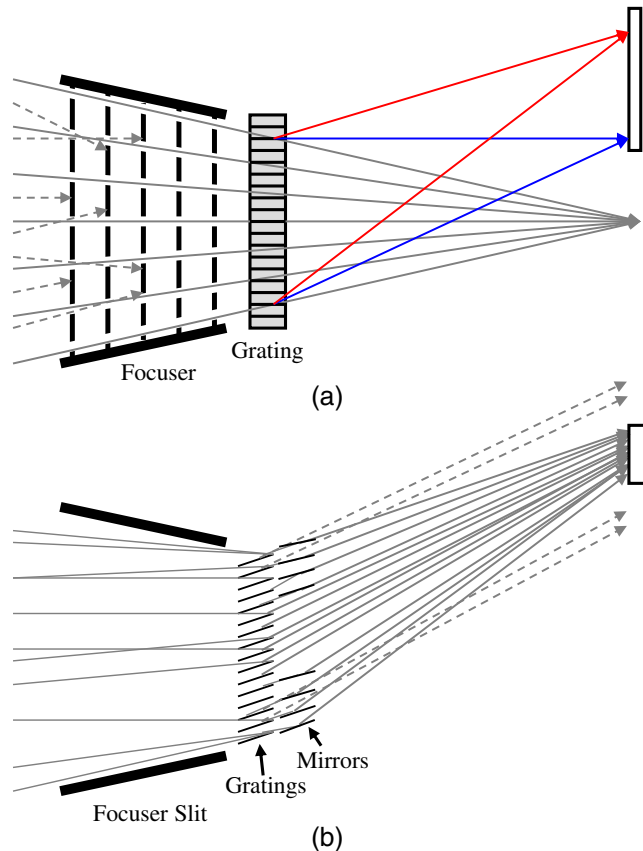

Fig. 2 (a) The mechanical focuser passively focuses light by occulting any photons that do not match the convergence of the focuser slits (dashed lines). The light that matches the convergence of the focuser forms a line focused in one dimension at the focal plane. Before reaching the focus, however, the light is intercepted and dispersed by reflection gratings. (b) A single focuser slit is shown in the orthogonal dimension to the top half of the diagram. In this dimension, a wider range of photon angles is allowed, resulting in an extended line at the focal plane. The array of reflection gratings diffracts the extended line, but the array or mirrors provide a second reflection to collapse the LSF in the extended direction onto a smaller area at the focal plane. The dashed lines show the light path if the mirrors were not present. Diagram is not to scale.[27]

introduced in Sec. 1.1 and is discussed in detail in Refs. 13 and 27. The focuser property that affected the design of the remainder of the payload was the size of the x-ray beam at the focuser's exit aperture, ~113 mm × 113 mm. The focused x-ray beam converged in one dimension and diverged in the other to produce an LSF at the focal plane with a width of ~2 mm FWHM[13] and a length of several hundred millimeters.

An array of x-ray reflection gratings was installed following the focuser to intercept and diffract x-rays into distinct spectral lines at the focal plane. The top half of the optical diagram in Fig. 2 shows a cross-section of the mechanical focuser followed by a reflection grating. The focuser occults any light that does not match the convergence of the slits. The light that is allowed to pass completely through the focuser forms a 1-D line focus at the focal plane. Prior to coming to that focus, however, the light is intercepted by the reflection gratings and dispersed according to its wavelength, as shown by the colored lines in the top half of Fig. 2. The WRXR reflection gratings leveraged development from the NASA Strategic Astrophysics Technology (SAT) program that supports research into high-resolution, highly efficient

Fig. 3 The WRXR flight grating module. 26 gratings were individually aligned into the module, each separated by ~3.8 mm. A small optical grating square is visible on the first grating in the array; optical gratings were used in the alignment process to constrain yaw.

Fig. 4 Cross-sectional view of a HCD. The Si absorbing layer is joined to a ROIC via in bump bonds.

gratings for future x-ray missions. To ensure the gratings covered the entire beam exiting the focuser, 26 gratings were coaligned into an array to cover the beam extent in one dimension and each grating was 110 mm wide to intercept the beam in the converging dimension. The gratings were 100 mm in the groove direction and 0.57 mm thick, each based on maximizing grating area and substrate fidelity within the constraints of 150-mm diameter silicon wafers, which were the substrates used for the WRXR gratings. Each grating in the array was replicated from a single "master" grating so that the flight array consisted of 26 identical grating copies. The gratings were aligned to within several arc minutes in pitch and ~1 arc min in roll and yaw, meeting the required tolerances.[28] Figure 3 shows the final flight module with all 26 gratings.

The master grating (and therefore each replica used in the final instrument) was fabricated with a groove density and blazed facet angle (Table 1) such that, once aligned into a specific geometry in the array, diffraction efficiency was maximized in orders chosen based on Vela's diffuse emission: third and fourth order OVII, second order CVI, and fourth order OVIII. The gratings were each coated with a layer of nickel to enhance reflectivity over the target bandpass. The fabrication of the master grating followed the processes in Ref. 29, and the grating replicas were produced using substrate-conformal imprint lithography (SCIL) at SCIL Nanoimprint Solutions.[30]

Table 1 Specifications for the WRXR gratings and mirrors.

	Gratings	Mirrors
Quantity	26	11
Reflective coating	Nickel	Nickel
Size	$110 \times 100 \times 0.5$ mm^3	$110 \times 100 \times 0.5$ mm^3
Nominal graze angle	2.2 deg	0.35 deg to 0.80 deg
Blaze angle	29.5 deg	—
Yaw angle	1.25 deg	—
Groove density	5750 grooves/mm	—
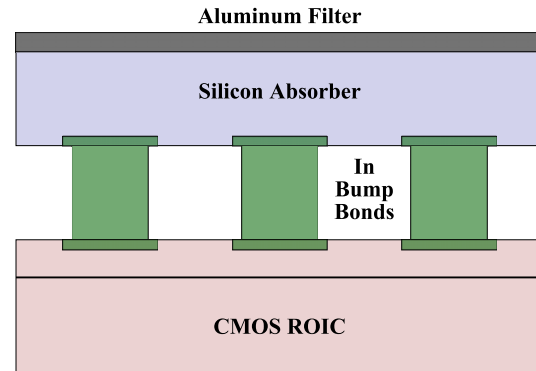
The detailed design of the WRXR gratings and mirrors is presented in Ref. 31, and the alignment of each grating into the array is discussed in Ref. 28.

Following the grating array was an array of flat, nickel-coated silicon mirrors. The bottom half of Fig. 2 depicts the focuser, gratings, and mirrors. A single focuser slit is shown in the axis orthogonal to the top half of the figure; along this axis, the slit converges from ~165 to ~113 mm, resulting in a much larger range of acceptance angles and a long line at the focal plane. The mirror array, shown edge-on following the grating array, was designed such that mirrors would intercept light on the edges of the diffracted beam and provide a secondary reflection to redirect light that would fall outside the detector active area at the focal plane. The flat mirrors redirected the diffracted beam by having a variable pitch angle, shifting the lines in the cross-dispersion direction to a smaller area at the focal plane. The mirrors were aligned with the same methodology as the gratings to ~1 arc min in yaw and roll, corresponding to <0.05 mm of aberration on the ~2 mm LSF.[28] The mirror array was expected to provide an additional ~20% flux onto the detector. However, a design flaw resulted in mirror positions in half of the array being incorrect by several hundred microns, which would cause the mirrors in that half of the array to effectively occult the diffracted beam rather than reflecting the light. Without sufficient development time to fabricate and align mirrors into a new array, the flawed array was flown with only half of the module populated, reducing the expected throughput gain by a factor of 2.

3 Hybrid CMOS Detector

An x-ray HCD, developed through a collaboration between PSU and Teledyne in an effort to fill the technology gap for high-performance imaging sensors on next-generation x-ray observatories, was used to image the spectrum produced by the optical components. The WRXR spectrometer provided the first testbed for a space-based demonstration of x-ray HCDs, a crucial step in the development of HCDs for future missions. The HCD used for the WRXR spectrometer was a specially modified, engineering-grade Teledyne HAWAII-2RG detector (H2RG), where the "2" refers to the size of the readout integrated circuit (ROIC) array in multiples of 1024 pixels, resulting in a 2048 × 2048 pixel array. The ROIC array, which has 18 μm pixel pitch, was bonded to a 1024 × 1024 silicon absorber array with 36 μm pixel pitch. The unique layout depicted in Fig. 4 was designed to reduce the effects of interpixel capacitance cross talk (IPC), which was an issue in the earlier generation of x-ray HCDs,
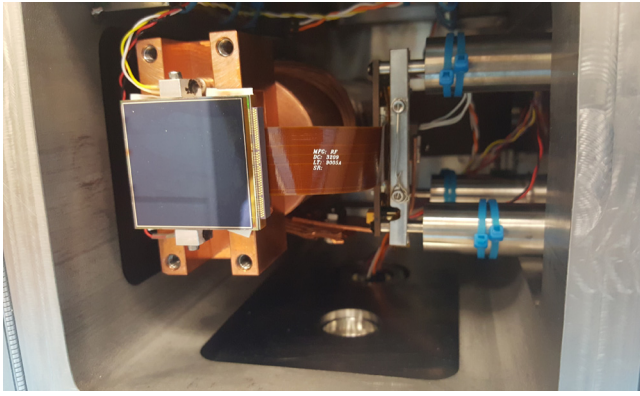
Fig. 5 The WRXR camera chamber with H2RG (at image left) and SIDECAR™, which is connected to the H2RG via the ribbon cable in the center of the chamber.

by increasing the distance between ROIC pixels (more recent x-ray HCDs do not suffer from IPC effects due to improved pixel amplifiers).

The WRXR H2RG was operated in conjunction with a Teledyne cryogenic application-specific integrated circuit, the SIDECAR™ ASIC, which provided driving voltages, managed image acquisition, and performed output digitization. The SIDECAR™ was controlled with a camera interface board (CIB) developed at PSU. The CIB powered, programmed, and controlled the SIDECAR™ and performed camera housekeeping, minor signal processing, and telemetry interfacing.

PSU designed and built a custom camera package (Fig. 5) to house the H2RG and SIDECAR™ for implementation in the WRXR spectrometer. Several application-specific features were added to the camera package for the suborbital rocket flight. The camera package was isolated from the rest of the instrument by a gate valve and utilized a dedicated ion pump to maintain low pressures during cooling operations. The gate valve and dedicated pumping solution allowed the camera package to operate independently of the vacuum status of the rest of the instrument and were intended to provide protection against pressure spikes before, during, and after launch. To obstruct optical and UV photons, which are often a source of background in space-based observations, while still allowing transmission of x-rays, a standalone Luxel filter was mounted ~6.5 mm in front of the detector. The filter used for the WRXR was a combination Al/Ti filter (65.7 nm Al and 42.2 nm Ti) that was supported with a nickel mesh. Additionally, a radioactive ^{55}Fe source was attached to the filter mount inside the camera chamber to constantly illuminate ~1/2 of the detector with hard (5.9 keV) x-rays. The ^{55}Fe source provided both a consistent calibration source and a detector diagnostic reference throughout ground testing and flight. Further details on the camera package, including thermal, electrical, and mechanical considerations, are provided in Ref. 32.

4 NASA Water Recovery Technology

In addition to the development of technologies targeted for future x-ray observatories, the WRXR payload provided a platform for the NASA Sounding Rockets Program to demonstrate water recovery technology for the first time with science payloads. Key adaptations included a sealed Celestial Attitude Control System (CACS) and a water-wedge equipped shutter door. The technologies enable recovery and re-flight of science

experiments and sounding rocket subsystems from aquatic landing zones, which further the Sounding Rocket Program Office's (SRPO) goals of providing low-cost access to space and opening additional launch sites to enable additional science targets.

The sealed CACS was responsible for all aspects of telescope pointing throughout flight: coarse orientation of the >1000 lb payload, settling onto the SNR, and arcsecond-level pointing stability. The CACS modifications included a repackaging of the high-pressure pneumatics system to preclude internal water damage to the electronics and enable re-flight of critical components. The system was hermetically sealed and provided additional ballast to the payload to enable floating stability leading to recovery.

The intent of the new water-recovery shutter door was to provide a shock absorber for the payload as it contacted the ocean surface on re-entry. The SRPO adapted design methodologies for crush bumpers used in traditional terrestrial recoveries to design a shutter-door-mounted water-wedge, which eased the payload's transition into the water by absorbing the impact from the initial contact. Once the payload's shutter door closed prior to re-entry into the atmosphere, the newly designed water-wedge became the aft-most section of the payload and absorbed energy from the impact with the ocean surface, protecting the science instrument.

In addition to the newly designed CACS and water wedge, the payload was outfitted with float bags to aid in buoyancy, global positioning sensors and strobe locator lights to assist in locating and tracking the payload in the ocean, and a hermetic telemetry section.

5 Preflight Calibrations and Performance

5.1 *Component-Level Measurements*

Prior to instrument buildup, calibration and optimization data were obtained for both the reflection gratings and the HCD; the mechanical focuser had flown on two previous instruments, and data from those instruments were used in place of new calibrations. Two gratings were randomly selected from the population used for the final flight array and tested for diffraction efficiency at Lawrence Berkeley National Laboratory's Advanced Light Source (ALS). The ALS experimental setup, data collection, and analysis followed the procedures discussed in Ref. 29. Figure 6 shows the absolute total and single-order diffraction efficiency from one of the gratings tested at the ALS.

The grating test geometries at the ALS differed slightly from the nominal WRXR geometry, which resulted in a small but noticable shift in single-order efficiency as a function of energy; this is evident in Fig. 6, where the intersection between third and fourth orders occurs at ~590 eV rather than ~570 eV as designed for OVII emission. Despite the slight shift in efficiency curves due to small deviations in test geometry, however, the total diffraction efficiency is representative of grating performance in similar orientations. Total absolute diffraction efficiency exceeds 70% at low energies and near the CVI emission energy (~375 eV) and is above 50% at OVII and OVIII (~570 and ~650 eV, repectively). Further, the efficiency curves demonstrate that the grating performance closely matches design; most of the efficiency at the desired energies is contained in individual orders: ~60% efficiency in second-order at CVI, ~50% efficiency split between third and fourth orders at OVII, and ~35% efficiency in fourth order at OVIII. The total diffraction efficiency of both gratings tested before the
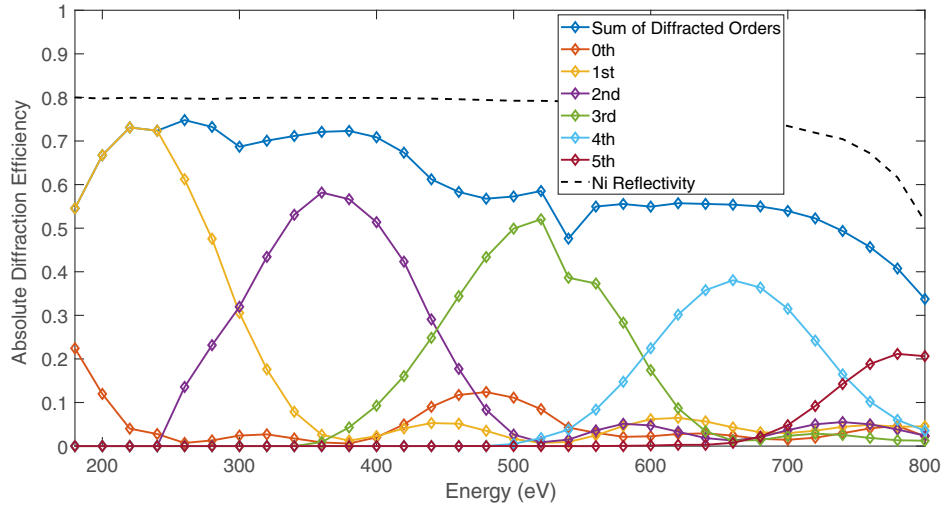
Fig. 6 The absolute diffraction efficiency of a WRXR grating measured before the flight. The black dashed line shows the reflectivity of nickel and sets the upper limit on possible diffraction efficiency. The blue solid line is the total measured diffraction efficiency (not including zero-order reflection). Each other line represents single-order diffraction efficiency.

flight is shown in Fig. 9. Finally, a grating coverage experiment was performed, where the diffraction efficiency was measured at 570 eV (near the OVII emission energy) as a function of position on the grating surface. The total area covered in the experiment was limited by stage travel to 80 mm × 80 mm (out of the 100 mm × 110 mm gratings). The diffraction efficiency of third and fourth orders at this energy (the two orders that are captured by the H2RG in the flight instrument) varied by ∼6% from position-to-position over the grating surface, and total diffraction efficiency (all orders other than 0th-order reflection) varied by <5%.

Similarly, the H2RG camera was calibrated independently before being integrated into the full instrument. Calibration runs consisted of several hundred integrations for which the data were processed with a typical x-ray analysis pipeline that included event thresholding and grading.[14] Extensive data were collected at various temperatures to compensate for temperature variations in flight; active cooling of the detector package ceased just prior to rocket liftoff, causing the temperature of both the detector and SIDECAR™ to drift during the course of flight. To simulate flight conditions, calibration data were obtained at a range of temperatures with the temperature held constant (conditions on the ground just prior to liftoff) and also in a series of "drift" runs in which active cooling was turned off and the detector and SIDECAR™ were allowed to warm naturally (conditions throughout the flight). Detector read noise and energy resolution as a function of temperature were obtained from the resulting data using a variety of calibration sources with unique energies in the x-ray bandpass: the ^{55}Fe source provided Mn-Kα x-rays at 5.9 keV, and a Po-210 alpha particle source fluoresced an Mg target mounted on Al to produce K-shell emission for O (0.53 keV), Mg (1.25 keV), and Al (1.49 keV). At the frame rate used in this instrument, the H2RG dark current became negligible below ∼170 K; preflight calibration, therefore, focused on determining the SIDECAR™ temperature that allowed the most optimal read noise.

Read noise was calculated as the average RMS pixel value of a sequence of dark images using the half of the H2RG that was not illuminated by ^{55}Fe x-rays. Results are summarized in

Table 2 Read noise of the H2RG measured as a function of temperature in preflight component-level testing.

SIDECAR™ temperature	H2RG temperature	Read noise
173 K	130 K	6.59 ± 0.03 e$^-$
179 K	140 K	8.06 ± 0.04 e$^-$
186 K	150 K	12.36 ± 0.06 e$^-$

Table 2 for several combinations of SIDECAR™ and H2RG temperatures. At SIDECAR™ temperatures in excess of 190 K, the noise introduced by the SIDECAR™ itself became high enough to completely saturate the OVII line (0.57 keV). To ensure noise levels sufficient to detect the target oxygen lines in flight, an optimal SIDECAR™ launch temperature was set at 173 K, corresponding to an H2RG temperature of 130 K.

Energy resolution was determined using Gaussian fits to the calibration spectra and was measured using single-pixel events for spectral lines below 2 keV and single- and two-pixel events for the 5.9 keV line; event grading selections were based on the availability of events in the flight data. Table 3 summarizes the FWHM energy resolution at different energies with the SIDECAR™ and H2RG cooled to 173 and 130 K, respectively.

5.2 Instrument-Level Calibrations

Following component-level optimization, the focuser, gratings, mirrors, detector, and all support equipment were built up into the complete spectrometer. The WRXR spectrometer had a focal length of ∼2 m and was designed to fit inside a 22-in. diameter cylindrical tube, which also provided the external mechanical structure for integration into the suborbital rocket package. The instrument electronics section and transition section aft of the spectrometer optics tapered from 22 to 17 in. to allow the instrument to fit into a standard suborbital rocket fairing (refer to Fig. 1).

Table 3 Energy resolution of the H2RG during preflight component-level and instrument-level testing. All data were collected at a SIDECAR™ temperature of ∼173 K and H2RG temperature of ∼130 K.

Energy	Resolution—component-level	Resolution—instrument-level
0.28 keV	—	109 ± 2 eV
0.39 keV	—	90 ± 2 eV
0.52 keV	89 ± 5 eV	88 ± 1 eV
1.25 keV	122 ± 4 eV	—
1.49 keV	110 ± 5 eV	—
5.90 keV	198 ± 10 eV	202 ± 3 eV

The aft end of the payload, the direction toward which the optics pointed, was fitted with a port to accommodate a bolt-on x-ray calibration source for ground testing. The calibration source used for the WRXR was an electron-impact source that produced x-rays by boiling electrons off of a tungsten filament and accelerating those electrons into an aluminum anode. With this method, K-shell emission was produced from C (0.28 keV), N (0.39 keV), and O (0.53 keV). Without the ability to produce the highly ionized states of oxygen and carbon that are observable in high-energy sources, such as the Vela SNR, K-shell emission of the associated elements was the most convenient way to calibrate the space-based instrument from the ground.

The x-ray calibration source directed a diverging beam of photons through the optics channel, producing a line that was then diffracted by the gratings, reflected by the mirrors (or allowed to pass freely through the mirror array depending on the photon positions), and imaged by the HCD. Placing diffracted orders of multiple energies on the detector during ground calibrations allowed for both positional measurements of optics-to-detector alignment and detector performance characterization. Figure 7 shows a 2-D histogram of x-ray counts from the three spectral lines produced with the electron-impact calibration source. Preflight, full-instrument H2RG energy resolution analysis yielded ∼109 eV at 0.28 keV, ∼90 eV at 0.39 keV, ∼88 eV at 0.52 keV, and ∼202 eV at 5.9 keV (Table 3). Read noise was measured each time independent instrument tests were performed, with the lowest noise measurement reaching 5.93 ± 0.02 e⁻ at the conclusion of preflight testing.
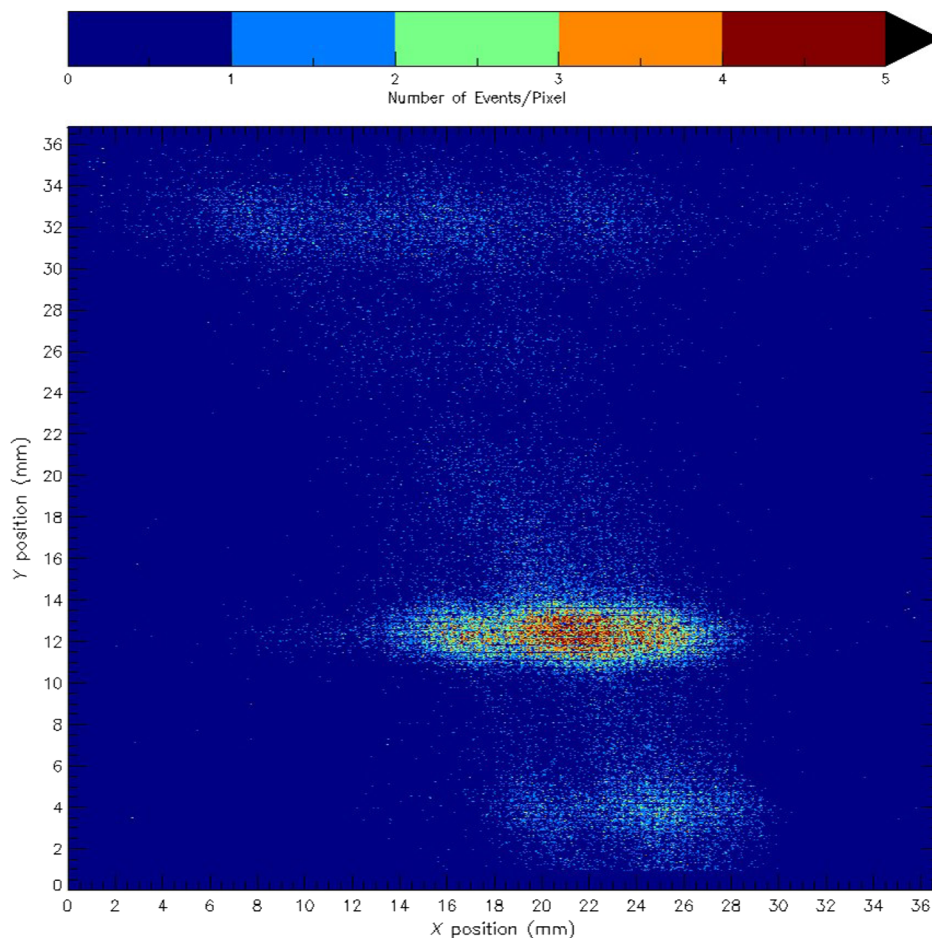

Fig. 7 A 2-D histogram of low-energy x-ray events imaged with the H2RG after being generated by an electron-impact source and passing through the full spectrometer. From top to bottom, the three spectral lines visible on the detector are second-order C-Kα, third-order O-Kα, and second-order N-Kα. The calibration lines do not cover the full cross-dispersion extent of the detector due to the nature of the calibration setup; the calibration source was mounted on the payload itself and was unable to fully illuminate the entrance aperture of the focuser.

6 Flight

6.1 Flight Plan

The nominal flight plan for the WRXR was developed to maximize time on the science target while still allowing for in-flight instrument calibration. Toward that goal, several features were implemented into the detector chamber design and flight control plan to provide flexibility during flight. First, the addition of the aforementioned ^{55}Fe calibration source provided a steady flux of x-rays onto the detector. Second, the gate valve that isolated the detector chamber from the main payload was controllable via an experiment command-uplink system, allowing for real-time actuation to either expose or protect the detector before, during, and after the flight. Finally, a pull-away liquid nitrogen cooling system was implemented to actively cool the detector until seconds before launch, providing control of H2RG and SIDECAR™ temperature leading up to flight.

After final rocket motor arming was completed ~2 h before launch, the camera was powered on and allowed to operate continuously until after the science observation in flight. At the time of liftoff, the H2RG and SIDECAR™ were at 124 and 177 K, respectively. At the time of camera shut down near the end of the flight, the H2RG had warmed to 133 K and the SIDECAR™ to 178 K, keeping both near the target temperatures discussed in Sec. 5.1. Continuous camera operation on the ground, during rocket ascent, throughout the science observation, and for ~30 s after the science observation allowed for data to be collected for final ground calibration information, flight dark frames, and flight calibration frames with the on-board ^{55}Fe source. With the presence of a constant calibration source throughout the flight, the ability to collect dark frames before and after the science observation, and the collection of dark sky images as the rocket slewed to the SNR, the WRXR successfully pointed at Vela for the entire duration of the allocated observation time without sacrificing calibration data. The total on-target observation time throughout the flight was 289 s.

6.2 Flight Data

Driven by an automated exposure cadence, the 289 s of on-target observation yielded ~280 s of active exposure on the Vela SNR. A processed image of all events near the OVII emission energy (0.57 keV) and a spectrum of those events are shown in Fig. 8. Analysis of the background in the spatial regions where spectral lines should have diffracted indicated that ~12 events were necessary in a given spectral line to obtain a 3σ detection of OVII x-rays from Vela. Though ~150 events are visible over the entire processed image area, there are no apparent spectral lines or preferential event positions. The spectrum further demonstrates that there are no OVII x-ray events that can be identified above the background with statistical significance. More in-depth analysis, including examinations of CVI and OVIII energies and of the regions on the detector at which the spectral lines should be present, yielded the same conclusion: there was no significant detection of soft x-ray emission from Vela during the WRXR flight. This conclusion motivated postflight instrument testing and calibration to determine if there were any unexpected instrument performance issues during flight or if a potential upper limit could be placed on emission from Vela.

6.3 Flight Anomaly

During the payload's ascent, the pressure measured by the WRXR pressure transducers increased by over an order of magnitude in the span of a few seconds as the payload ascended through the atmosphere. As designed, the gate valve that isolated the detector chamber should have protected the cold (124 K at launch) detector from this pressure spike. However, weather-induced payload damage experienced in the days leading up to launch necessitated a modified flight plan; a sudden rain shower during launch readiness testing damaged the detector chamber's ion pumping system (discussed in Sec. 3) beyond repair. As a result, the detector chamber lacked a dedicated vacuum pump. To compensate for the ion pump failure, the payload was launched with the gate valve open, exposing the detector to
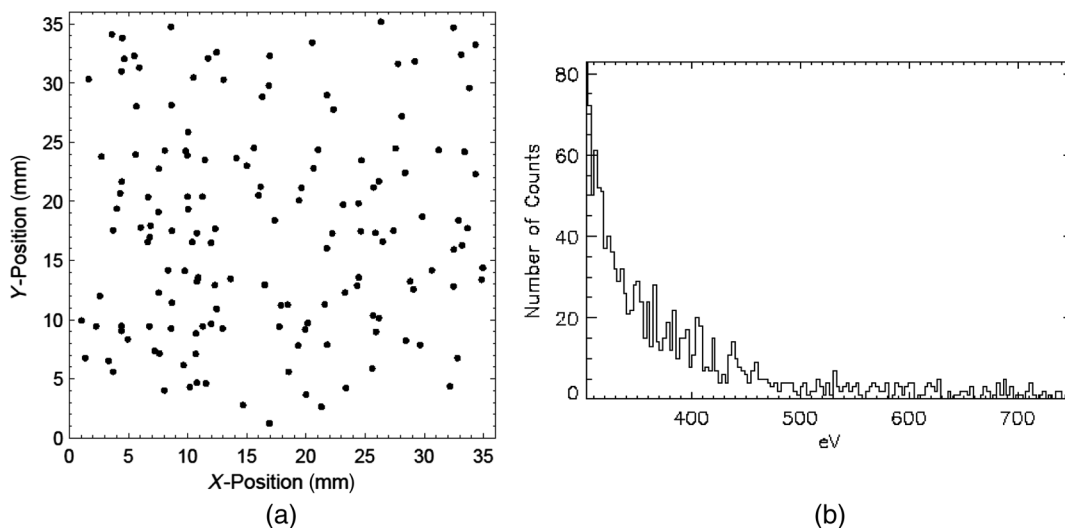

Fig. 8 All events detected during the flight observation that satisfied image processing and OVII-thresholding limitations. (a) A scatter plot of the position on the detector of each event and (b) an energy spectrum of all events. The spectrum shows a low-energy background and is flat near the OVII energy (570 eV) with no indication of significant OVII x-ray events.

the main instrument earlier than designed but allowing the low pressure of the main instrument to act as a getter for the detector chamber. However, the pressure spike that the payload experienced as it ascended through the atmosphere subjected the cold detector to higher-than-desirable pressure and likely deposited a condensation layer on the detector surface, a possibility discussed further in Sec. 7.2.

7 Postflight Analysis

7.1 Component Verification

The two primary objectives of postflight component verification were to measure diffraction efficiency of the gratings and the performance of the H2RG after both experienced a suborbital rocket flight. At the completion of instrument-level testing, the reflection grating array was uninstalled from the instrument and a grating was removed. The disassembled grating was then taken again to the ALS for a similar diffraction efficiency experiment. The results, summarized in Fig. 9, were consistent with preflight performance to within the variation measured in the grating coverage experiment (~5%). The postflight grating efficiency experiment provided verification that the gratings maintained their fidelity throughout exposure to launch conditions, space, and recovery efforts. Similarly, H2RG read noise and energy resolution were again measured under the same temperature conditions, yielding 6.47 ± 0.06 e$^-$ read noise and 212 ± 4 eV energy resolution at 5.9 keV. A comparison of postflight detector measurements to both preflight and flight data is summarized in Table 4.

7.2 Condensation Analysis

After verifying that the instrument alignment held throughout the flight and that the individual components maintained their performance levels, postflight analysis moved to the most critical investigation: the expected significance of the pressure spike experienced during the payload's ascent to space. Extensive testing was performed in an effort to re-create the flight conditions to directly observe the effects on x-ray transmission. The

Table 4 A comparison of read noise and energy resolution at the 5.9 keV Mn-Kα line produced with the ^{55}Fe radioactive decay source for preflight testing, flight performance, and postflight testing.

H2RG performance in WRX spectrometer		
	Read noise	Energy resolution at 5.9 keV
Preflight component level	6.59 ± 0.03 e$^-$	198 ± 10 eV
Preflight instrument level	5.93 ± 0.02 e$^-$	202 ± 3 eV
Flight	6.25 ± 0.04 e$^-$	193 ± 5 eV
Postflight instrument level	6.47 ± 0.06 e$^-$	212 ± 4 eV

experiment that was determined to be representative of the flight anomaly began with frozen water inside a tube that was connected to the camera chamber, which was under vacuum to best simulate flight conditions. The ice was then allowed to melt, resulting in pure water vapor that was then allowed to condense onto the detector surface. The water vapor volume and pressure used in postflight testing were the best approximation to the conditions experienced in flight to expose the detector to the same amount of water vapor; the increase in pressure during flight is believed to have been caused by the external skin heating and outgassing water, and the postflight experiment sought to match the pressure of water available to condense onto the detector. After the condensation layer was deposited, H2RG x-ray flux levels were measured and compared with pre-exposure measurements with the same source flux. Table 5 summarizes the results of the test, which demonstrated heavy attenuation of all x-rays and ~85% attenuation at O-Kα (the closest line in energy to the dominant emission lines from the Vela SNR), and Fig. 10 shows x-ray flux before and after the condensation layer was added to the detector. An estimate of the condensation layer required to attenuate x-rays to the observed level yielded a thickness of 17.5 ± 1.5 μm. Figure 11 shows the transmission of soft x-rays
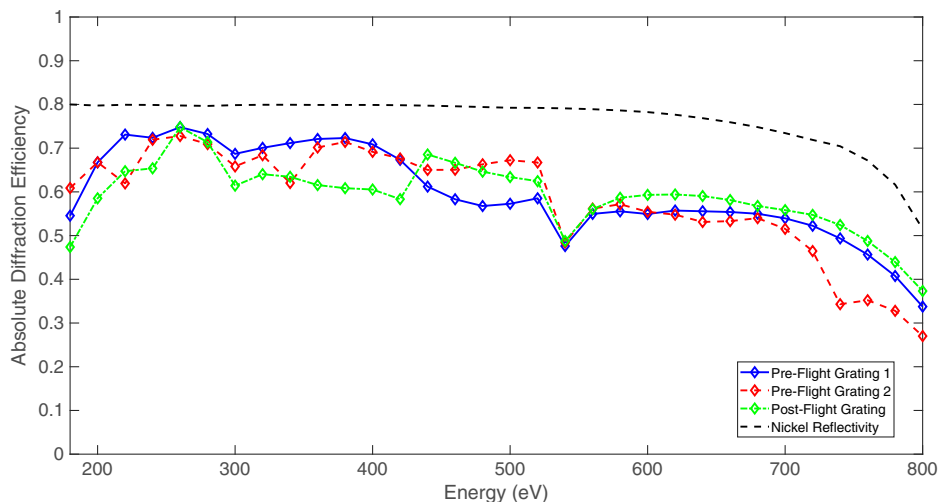

Fig. 9 The total absolute diffraction efficiency of three WRXR gratings. Two gratings were tested before the flight and a third grating was uninstalled from the flight array and tested as part of postflight calibrations. Though there are slight deviations in total diffraction efficiency from grating to grating, which is partially a product of unique test configurations, the total efficiency as a function of energy is consistent in all gratings measured.

Table 5 A summary of the postflight condensation experiment where the camera was subjected to approximately the same level of water vapor as during the flight. The attenuation of x-rays at each distinct energy is consistent with a layer of condensation of ~17.5 μm thick.

	O	Na	Mg	Al
Energy	0.52 keV	1.05 keV	1.25 keV	1.49 keV
Precondensation counts	1785	3215	8170	8796
Postcondensation counts	269	0	181	585
Flux loss	85%	100%	98%	93%

through a 17.5 μm thick layer of water, demonstrating that a condensation layer of comparable thickness could have effectively eliminated the expected x-ray counts from Vela during flight and prevented any conclusions about Vela's soft x-ray emission.

8 Conclusions

The suborbital rocket payload WRXR flew a soft x-ray spectrometer that demonstrated the space performance of x-ray reflection gratings and an x-ray HCD, both of which are technologies being developed for future space missions. The WRXR also provided the first demonstration of NASA sounding rocket water recovery technology, enabling the recovery of science
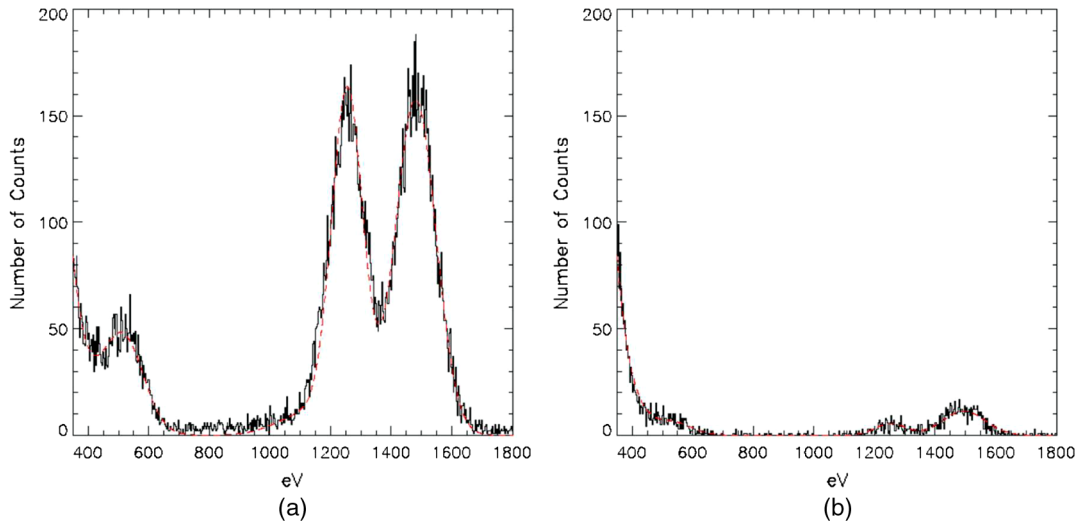

Fig. 10 Results of the postflight condensation test for O, Mg, and Al x-ray lines. (a) Before condensation and (b) after condensation, with equal exposure times. X-rays of all energies are almost entirely attenuated by the condensation layer.
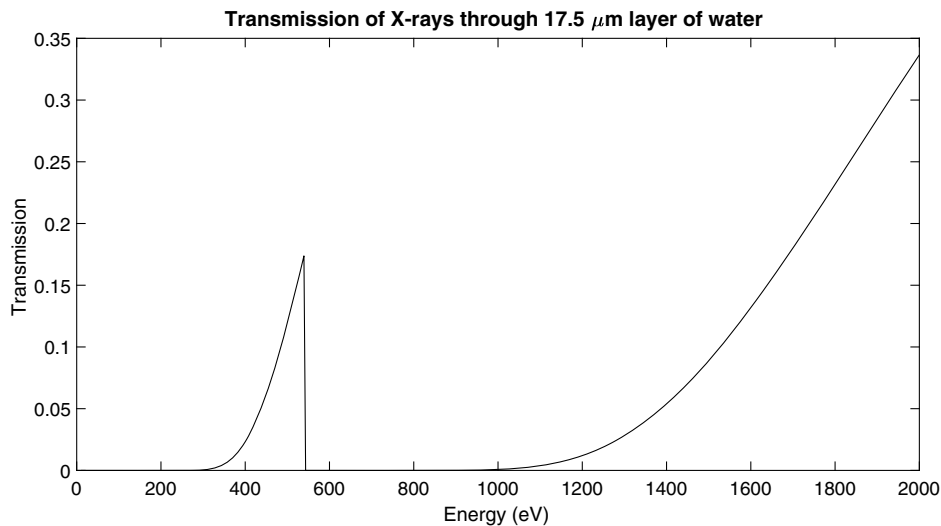

Fig. 11 The transmission of x-rays through a 17.5-μm thick layer of water.[33] The dominant emission lines from Vela (CVI at ~370 eV, OVII at ~570 eV, and OVIII at ~650 eV) would all be almost entirely occulted by such a layer.

payloads from aquatic environments and the opening of new launch sites for science programs. Although a combination of low source flux and possible condensation on the detector during flight prevented the WRXR spectrometer from obtaining observational constraints on the Vela SNR, instrument performance was a significant development step in technology maturation and as a pathfinder for upcoming suborbital payloads.

References

1. National Aeronautics and Space Administration, "Astrophysics Biennial Technology Report," https://apd440.gsfc.nasa.gov/images/tech/ABTR_print_2019.pdf (2019).
2. R. McEntaffer, "Reflection grating concept for the Lynx x-ray grating spectrograph," *J. Astron. Telesc. Instrum. Syst.* **5**(2), 021002 (2019).
3. S. Hull et al., "Hybrid CMOS detectors for the Lynx x-ray surveyor high definition x-ray imager," *J. Astron. Telesc. Instrum. Syst.* **5**(2), 021018 (2019).
4. A. D. Falcone et al., "Overview of the high definition x-ray imager (HDXI) on the Lynx x-ray surveyor," *J. Astron. Telesc. Instrum. Syst.* **5**(2), 021019 (2019).
5. R. K. Smith et al., "Arcus: an ISS-attached high-resolution x-ray grating spectrometer," *Proc. SPIE* **9144**, 91444Y (2014).
6. M. W. Bautz et al., "Concepts for high-performance soft x-ray grating spectroscopy in a moderate-scale mission," *Proc. SPIE* **8443**, 844315 (2012).
7. R. McEntaffer and R. Smith, "The x-ray grating spectrograph probe (XGS-P)," The Space Astrophysics Landscape for the 2020s and Beyond (2019).
8. A. D. Falcone, "X-ray hybrid CMOS detectors in astronomy," in *The WSPC Handbook of Astronomical Instrumentation*, D. N. Burrows, Ed., World Scientific Publishing Company, Singapore (2020).
9. B. Donovan et al., "Optical design of the off-plane grating rocket experiment," *Proc. SPIE* **10699**, 106993U (2018).
10. D. M. Miles et al., "An introduction to the Rockets for Extended-source X-ray Spectroscopy," *Proc. SPIE* **11118**, 111180B (2019).
11. T. Chattopadhyay et al., "BlackCAT CubeSat: a soft x-ray sky monitor, transient finder, and burst detector for high-energy and multimessenger astrophysics," *Proc. SPIE* **10699**, 106995S (2018).
12. N. Kruczek et al., "The fourth flight of CHESS: spectral resolution enhancements for high-resolution FUV spectroscopy," *Proc. SPIE* **10699**, 106990K (2018).
13. B. Zeiger, "Soft x-ray spectroscopy of the Vela supernova remnant," Doctoral Thesis, University of Colorado (2012).
14. Z. Prieskorn et al., "Characterization of Si hybrid CMOS detectors for use in the soft x-ray band," *Nucl. Instrum. Methods Phys. Res.* **717**, 83–93 (2013).
15. A. D. Falcone et al., "Hybrid CMOS x-ray detectors: the next generation for focused x-ray telescopes," *Proc. SPIE* **6686**, 668602 (2007).
16. A. N. Cha, K. R. Sembach, and A. C. Danks, "The distance to the Vela Supernova remnant," *Astrophys. J.* **515**, L25–L28 (1999).
17. R. L. McEntaffer and T. Bransteg, "Chandra imaging and spectroscopy of the eastern XA region of the Cygnus Loop supernova remnant," *Astrophys. J.* **730**, 99 (2011).
18. R. L. McEntaffer and W. Cash, "Soft x-ray spectroscopy of the Cygnus loop supernova remnant," *Astrophys. J.* **680**, 328–335 (2008).
19. F. D. Seward et al., "X-rays from Puppis A and the vicinity of Vela X," *Astrophys. J.* **169**, 515–524 (1971).
20. P. Gorenstein, F. R. Harnden, and W. H. Tucker, "The x-ray spectra of the Vela and Puppis supernova remnants and the shock-wave model of supernova remnants," *Astrophys. J.* **192**, 661–676 (1974).
21. W. Burkert et al., "Soft x-ray filter spectroscopy of the supernova remnants VELA X and Puppis A," *Astron. Astrophys.* **115**(1), 167–170 (1982).
22. S. M. Kahn et al., "Einstein observations of the Vela supernova remnant: the spatial structure of the hot emitting gas," *Astrophys. J.* **299**, 821–827 (1985).
23. B. Aschenbach, R. Egger, and J. Trumper, "Discovery of explosion fragments outside the Vela supernova remnant shock-wave boundary," *Nature* **373**, 587–590 (1995).
24. A. Bamba, R. Yamazaki, and S. Hiraga, "Chandra observations of the galactic supernova remnant Vela Jr.: a new sample of thin filaments emitting synchrotron x-rays," *Astrophys. J.* **632**, 294–301 (2005).
25. T. J. Gaetz et al., "X-ray observations of the Vela supernova remnant ejecta fragments," *AIP Conf. Proc.* **1156**, 236–240 (2009).
26. F. J. Lu and B. Aschenboch, "Spatially resolved spectroscopy of the Vela supernova remnant," *Astron. Astrophys.* **362**, 1083–1092 (2000).
27. P. H. H. Oakley, R. L. McEntaffer, and W. Cash, "A suborbital payload for soft x-ray spectroscopy of extended sources," *Exp. Astron.* **31**(1), 23–44 (2011).
28. J. H. Tutt et al., "Grating alignment for the Water Recovery X-Ray Rocket (WRXR)," *J. Astron. Instrum.* **8**(2), 1950009 (2019).
29. D. M. Miles et al., "Grating design for the Water Recovery X-Ray Rocket," *Proc. SPIE* **10699**, 106996K (2018).
30. M. A. Verschuuren et al., "AutoSCIL 200 mm tooling in production, x-ray optics, and cell growth templates," *Proc. SPIE* **10584**, 105840Z (2018).
31. D. M. Miles et al., "Fabrication and diffraction efficiency of a large-format, replicated x-ray reflection grating," *Astrophys. J.* **869**, 95 (2018).
32. M. Wages et al., "Flight camera package design, calibration, and performance for the Water Recovery X-ray Rocket mission," *Proc. SPIE* **11118**, 111180D (2019).
33. B. L. Henke, E. M. Gullikson, and J. C. Davis, "X-ray interactions: photoabsorption, scattering, transmission and reflection at E=50-30000 eV, Z=1-92," *At. Data Nucl. Data Tables* **54**(2), 181–342 (1993).

Drew M. Miles is a PhD student at Pennsylvania State University. He received his BS degree in physics and astronomy from the University of Iowa in 2015. In addition to x-ray suborbital investigations, such as the WRXR, he fabricates reflection gratings and is researching new methods to produce high-performance gratings for future missions. He is a member of SPIE.

James H. Tutt is an assistant research professor at Penn State University. He completed his PhD at the Open University in the United Kingdom and is an expert in the use of silicon-based detectors in x-ray instruments. Since moving to the United States in 2014, he has been working on the design, build, and launch of x-ray spectrometers on suborbital rocket payloads.

Mitchell Wages is a research and development engineer at Pennsylvania State University. He received his BS degree in astronomy and astrophysics from Pennsylvania State University in 2016. He is a member of AAS. His interests include x-ray instrumentation, vacuum technologies, and mechanical design.

Benjamin D. Donovan is a graduate student at Pennsylvania State University. Prior to graduate school, he attended the University of Iowa, where he received his undergraduate degrees in physics and astronomy in 2016. His current research interests include the design, testing, and implementation of high-performance soft x-ray spectrometers. He is a member of SPIE.

Abraham D. Falcone is a research professor of astronomy and astrophysics at Pennsylvania State University. He received his BS degree

in physics from Virginia Tech in 1995 and his PhD in physics from the University of New Hampshire in 2001. He has authored 200 refereed journal publications. He leads research in fields ranging from x-ray and gamma-ray instrumentation to the study of particle acceleration at high-energy astrophysical sites, such as active galactic nuclei, gamma ray bursts, and x-ray binaries.

Tyler Anderson is an associate research professor at Pennsylvania State University. He received his PhD from Pennsylvania State University in 2013. He works on the design, characterization, and commissioning of high-performance, low-noise electronic instrumentation, and control systems for use in scientific and measurement applications.

Evan Bray is a graduate student at Pennsylvania State University, currently working toward a PhD in astronomy and astrophysics. He conducts research on the characterization of x-ray hybrid CMOS detectors (HCDs) and their applications to future x-ray space telescopes. His research includes experimental measurement and numerical simulation of subpixel spatial resolution as well as radiation damage on HCDs.

Biographies for the other authors are not available.